scientific reports

Check for updates

OPEN

Columnar excitation fluorescence microscope for accurate evaluation of quantum properties of color centers in bulk materials

Yuta Masuyama[1]✉, Chikara Shinei[2], Shuya Ishii[1], Hiroshi Abe[1], Takashi Taniguchi[2], Tokuyuki Teraji[2] & Takeshi Ohshima[1]

Color centers in wide band-gap semiconductors, which have superior quantum properties even at room temperature and atmospheric pressure, have been actively applied to quantum sensing devices. Characterizing the quantum properties of the color centers in the semiconductor materials and ensuring that these properties are uniform over a wide area are key issues for developing quantum sensing devices based on color centers. In this article, we have developed an optics design protocol optimized for evaluating the quantum properties of color centers and have used this design approach to develop a new microscopy system called columnar excitation fluorescence microscope (CEFM). The essence of this system is to maximize the amount of fluorescence detection of polarized color centers, which is achieved by large-volume and uniform laser excitation along the sample thickness with sufficient laser power density. This laser excitation technique prevents undesirable transitions to undesirable charge states and undesirable light, such as unpolarized color center fluorescence, while significantly increasing the color center fluorescence. This feature enables fast measurements with a high signal-to-noise ratio, making it possible to evaluate the spatial distribution of quantum properties across an entire mm-size sample without using a darkroom, which is difficult with typical confocal microscope systems.

Color centers such as NV centers in diamonds are expected to be an important tool for quantum sensing because they are qubits that can be operated at room temperature and atmospheric pressure[1–4]. In addition to NV centers in diamond, various other color centers, such as silicon vacancies in SiC[5,6], are beginning to be used depending on the sensing target application[7]. Magnetic sensing using quantum properties of NV centers has achieved the sensitivity of less than 1 pT/sqrt (Hz) by applying a large sensor volume[8,9]. Increasing the number of color centers increases sensor sensitivity, but increasing the density of donors such as color centers and nitrogen increases dipolar coupling, limiting sensitivity. To improve sensitivity, achieving a large sensor volume with high uniformity and weak dipole coupling is necessary[10]. Furthermore, equalizing the quantum properties of each sensor is crucial for multi-quantum sensor systems such as gradiometers , and it further enhances the performance of the sensors[11,12]. Therefore, for even higher sensitivity, uniform, high-quality sensor materials that allow large sensor volumes are required, and the methods for their evaluation are also important.

Confocal microscopy (CFM), wide-field imaging, and electron spin resonance (ESR) are methods capable of measuring the quantum properties of color centers. Each method and the CEFM proposed in this study play a significantly different role. CFM is a measurement technique with excellent spatial resolution, making it ideal for evaluating a small number of color centers. However, the small detection volume limits the fluorescence signal, extending each point's measurement time. Consequently, using CFM to measure the spatial distribution of quantum properties across the entire sample requires sampling a limited number of points in the spatial distribution and predicting the characteristics outside the measurement area. Wide-field imaging allows single-observation spatial distribution measurements[13–17]. Measuring quantum properties requires pulse measurements that need higher laser and microwave power density than continuous wave (CW) measurements (see "Supplemental material" for details). The measurement area for the pulse measurements is typically limited to a square, with each side approximately 100 µm long[18–20], necessitating stage movement for larger areas. Moreover, because fluorescence

[1]National Institutes for Quantum Science and Technology, Takasaki, Gunma 370-1292, Japan. [2]National Institute for Materials Science, Tsukuba, Ibaraki 305-0044, Japan. ✉email: masuyama.yuta@qst.go.jp

is split into individual pixels and stray light reduction is challenging, the signal-to-noise ratio per pixel is less than that of methods using a single detector in conjunction with a pinhole or optical fiber. ESR is a method that evaluates the quantum properties of the entire sample as an average value and is not suitable for evaluating the spatial distribution of quantum properties. To obtain a guideline for improving sensitivity, a method that can evaluate the spatial distribution of quantum properties in the sensor materials within a millimeter-order spatial range is desired.

In this study, we describe a design protocol for an optical system that realizes a measurement system capable of evaluating a wide spatial distribution of quantum properties of color centers and their concentration. We introduce a newly developed fluorescence microscope system featuring a uniform columnar excitation along the sample thickness (columnar excitation fluorescence microscope: CEFM) with an instrument configuration similar to a CFM system. The optical system designed using the method in this study allows for the injection of a laser beam that is axially uniform throughout the sample and has a relatively large spot size, resulting in a much larger detection volume. This uniform, significant volume excitation prevents transitions to unwanted color center charge states and unwanted light, such as fluorescence of unpolarized color centers, surface light, and background light, enabling sensitive evaluation of the quantum properties of color centers without using a dark room. Our proposed CEFM method can evaluate the spatial distribution of the quantum properties of an ensemble of color centers across mm-sized samples in a wide range of concentrations from about one ppb to more than ten ppm.

Results and discussion

Columnar excitation fluorescence microscope (CEFM)

CEFM is characterized by axially uniform optical excitation throughout the sample with a broader laser spot diameter than CFM. This feature significantly increases the amount of fluorescence in the color center to be detected while reducing unnecessary light that drops the signal-to-noise ratio caused by non-uniformity in optical power density. This unwanted light is emitted for the following reasons. Transitions to color centers with different charge states are promoted in regions with locally strong optical power density. On the other hand, in regions where the optical power density is locally weak, the color centers are not polarized, and fluorescence without quantum state information is emitted. Figure 1 shows a schematic diagram for comparison with existing color center evaluation methods. The spatial resolution, which correspond to the sample volume to be measured, of CEFM is inferior than that of CFM while better than that of ESR. In the practical use, CEFM is suitable for obtaining spatial distribution mapping of quantum properties across the entire mm-size sample. The proposed method polarizes spin states as efficiently as CFM. In addition, CEFM beam excites a larger area of the sample surface than CFM, but because it excites uniformly along the sample thickness, the ratio of excitation volume to surface area is relatively reduced, reducing stray light effects due to impurities on the surface. Eventually, the measurement time becomes very short when using CEFM. In our paper, we discuss the case of a single photodetector, such as an Avalanche Photodiode (APD), in a confocal optical setup. However, by optimizing the optical power density, as demonstrated in our study, it is also possible to employ an image sensor for measurements. Both

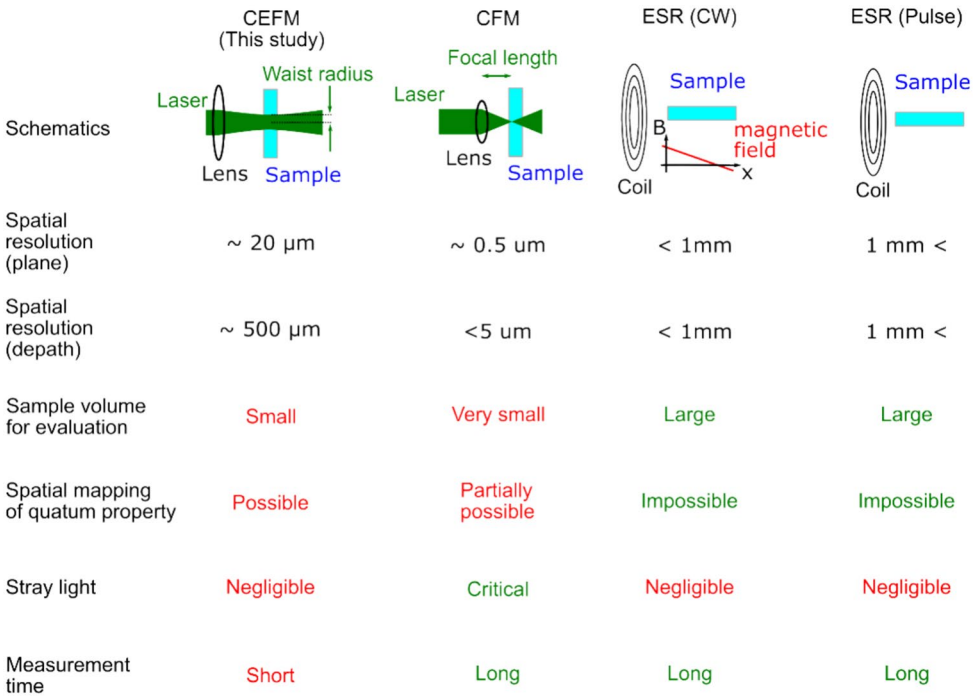

Figure 1. Comparison of this study with confocal microscopy (CFM) and electron spin resonance (ESR).

wide-field imaging and CEFM aim to measure the spatial distributions of the target. From a quantum properties measurement perspective, wide-field imaging excels at high-resolution measurements within a square, with each side approximately 100 μm long. On the other hand, CEFM sacrifices spatial resolution slightly but can cover a broader range in the millimeter scale with a high signal-to-noise ratio without a dark room. Details of features of CEFM are described below.

Rayleigh length and excitation volume

First, the optical features of this study are described. Figure 2a shows a schematic comparison of the beam diameter of CEFM and CFM. CFM typically uses a lens system with a high-magnification objective, whereas CEFM uses a low-magnification objective. This low-magnification lens allows for relatively large laser beam diameters of approximately 20 μm and axially uniform color-center excitation throughout the sample. The Rayleigh length is used as a measure of laser depth. The Rayleigh length z_R is the length from the focal point to the point where the beam radius is $\sqrt{2}$ times the waist radius w_0 which is beam radius at the focal point of the laser. And the Rayleigh length is defined as

$$z_{\mathrm{R}} = \frac{\pi w_0^2}{\lambda}, \tag{1}$$

where λ is the wavelength of the laser (Fig. 2b)[21]. Increasing the beam waist radius allows laser irradiation with a long Rayleigh length.

In this study, the calculations were made by approximating the laser excitation region as a cylindrical shape [the shaded area in Fig. 2c] (see "Supplemental material" for details). The average power density of the laser light passing through this cylinder is $\frac{P_0}{\pi w_0^2}$, where P_0 is the total power of the laser. A 50 × objective lens, which has an effective focal length of 3.6 mm, is commonly used in the case of CFM systems, as shown in Fig. 2c. When twice the Rayleigh length $2Z_R$ is shorter than the sample thickness, a cylinder of length (indicated by "Rayleigh length" in the Fig. 2) 2 z_R and waist radius w_0 is taken as the excited volume in the calculation. On the other hand, when twice the Rayleigh length $2Z_R$ is longer than the thickness of the sample, the calculation was done using the thickness of the sample as the length of the cylinder. As the laser beam waist radius increases, the laser excitation

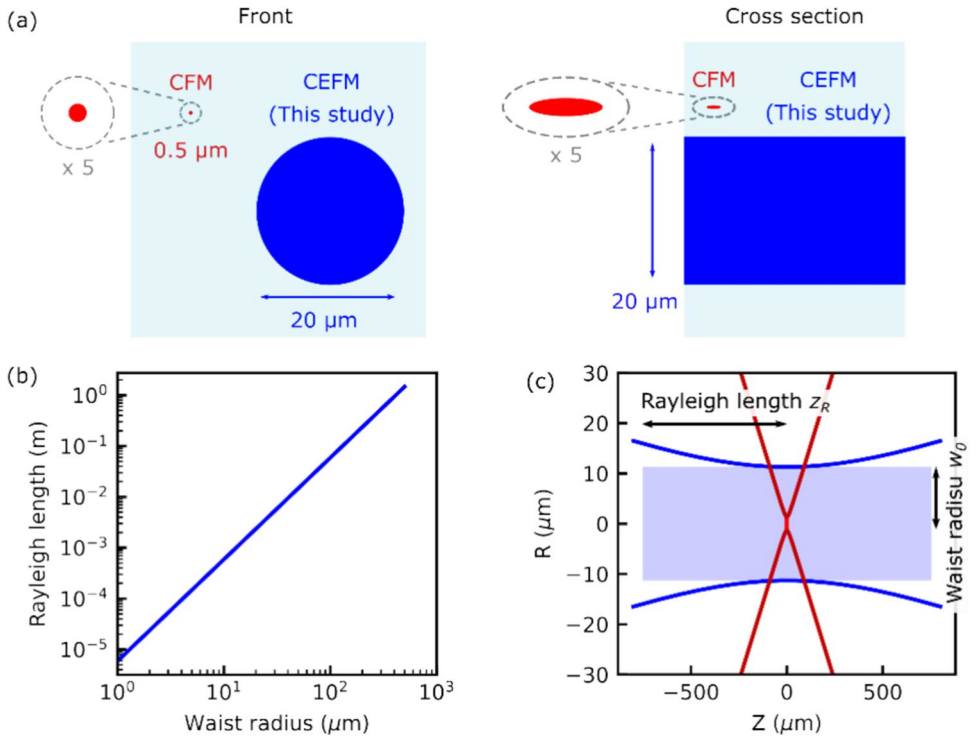

Figure 2. (**a**) Schematic comparison of this study (CEFM) and a confocal microscope (CFM) system. As we will show in this paper, matching twice the Rayleigh length $2Z_R$ to the thickness of the sample, corresponding to a columnar optical excitation to the sample, maximizes effective fluorescence detection. (**b**) Dependence of Rayleigh length on waist radius for laser wavelength 532 nm. (**c**) Excitation volume along the optical axis direction for focal lengths of 3.6 mm (red) and 30 mm (blue). The effective focal length of 3.6 mm corresponds to a 50 × objective lens, and the focal length of 30 mm is used in this study. The blue and red colored squares with twice the Rayleigh length $2Z_R$ and twice the waist radius on each side represent the effective beam areas with focal lengths of 30 mm and 3.6 mm, respectively.

volume rapidly increases. In the calculations below, the sample thickness of 500 μm and the incident 532 nm laser beam radius of 450 μm were applied.

The amount of detected light was evaluated to find the optimal laser beam condition for the CEFM. Specifically, the excitation volume was calculated by changing the Rayleigh length of the excitation laser, and then the amount of fluorescence emitted by polarized color centers within this excitation volume and the amount of collected light were evaluated. Here, these calculations were performed using the energy levels of the negatively charged NV centers in the diamond (Fig. 3) (see "Supplemental material" for details). The values of the transition rates of the NV center required for this numerical calculation were taken from the reference by[22].

The calculation step consists of two parts: one for the excitation of the NV centers and the other for detecting the fluorescence of the NV centers. We consider the Rayleigh length dependence of all the calculations to compare the calculation results well. The beam shape and optical power density change as the Rayleigh length varies. We calculate this effect for the excitation by decomposing the Rayleigh length dependence of the excitation volume, total fluorescence, and polarization ratio. The focal length of the lens controls Rayleigh length. Therefore, we calculate the Rayleigh length dependence of the Rayleigh length of the correction rate of the fluorescence of the NV center. Each of these calculations is described in detail below.

Excitation signal amount

When the waist radius is very large, the Rayleigh length increases but the laser power density decreases greatly, resulting in a significant decrease in the polarization ratio of the color center. This phenomenon is confirmed from the numerically calculated amount of fluorescence emitted from the region excited by the laser beam. Figure 4 shows the calculated results for the NV center.

The amount of fluorescence emitted from the NV center is calculated using the steady-state population in states $|3>$ and $|4>$ as

$$I_{CW} = \frac{k_{31} + k_{32}}{k_{31} + k_{32} + k_{35}} \rho_{33}^{ss} + \frac{k_{41} + k_{42}}{k_{41} + k_{42} + k_{45}} \rho_{44}^{ss}, \tag{2}$$

where ρ_{33}^{ss} and ρ_{44}^{ss} are the elements of the steady state density matrix corresponding to the states $|3>$ and $|4>$ and k_{ij} is the transition rate from level i to level j (see "Supplemental material" for details)[23]. Figure 4a shows the numerical results of the Rayleigh length dependence of the excitation volume at a laser power of 10 mW. The solid blue line corresponds to a sample with a thickness of 500 μm, and the dashed red line corresponds to a sample with infinite thickness. As shown in Fig. 4b, the fluorescence per unit volume decreases due to the lowering of laser beam power density.

The polarization ratio of a color center is an important indicator because a quantum state cannot be manipulated or read out unless it is polarized. The polarization ratio of a quantum state is defined as

$$P = \frac{\rho_{11}^{ss} - \rho_{22}^{ss}}{\rho_{11}^{ss} + \rho_{22}^{ss}}, \tag{3}$$

where ρ_{11}^{ss} and ρ_{22}^{ss} are the elements of the steady state density matrix corresponding to the states $|1>$ and $|2>$. In Fig. 4c, The polarization ratio at a laser power of 10 mW is calculated. According to the Eq. (1), there is a positive correlation between the laser beam diameter and the Rayleigh length. The polarization ratio decreases with increasing beam diameter that can be written with the Rayleigh length because the laser beam power density becomes lower [Fig. 4c, inset)].

Furthermore, we study the total signal volume effective for quantum state readout. We calculated the dependence of the product of the detection volume ($=\pi \times w_0^2 \times$ sample thickness), the fluorescence per unit volume I_{cw}, and the polarization ratio P on the Rayleigh length at a laser power of 10 mW (Fig. 4d). The polarization ratio

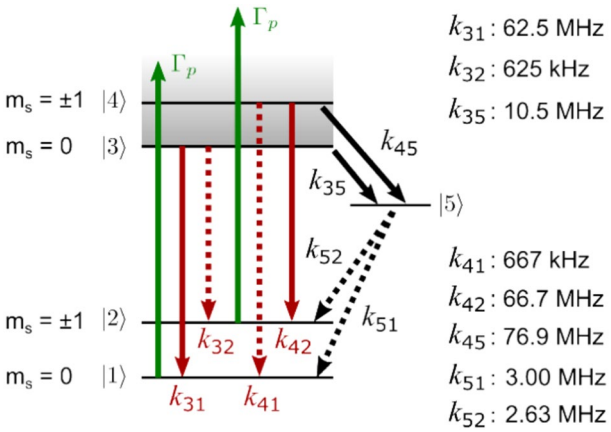

Figure 3. Energy level diagram for the NV center in diamond. The green arrow indicates optical excitation from the ground state of the NV center. The red arrow indicates fluorescence from the excited state of the NV center. m_s is magnetic sublevel of the NV center. k_{ij} indicates the transition rate from level i to level j.

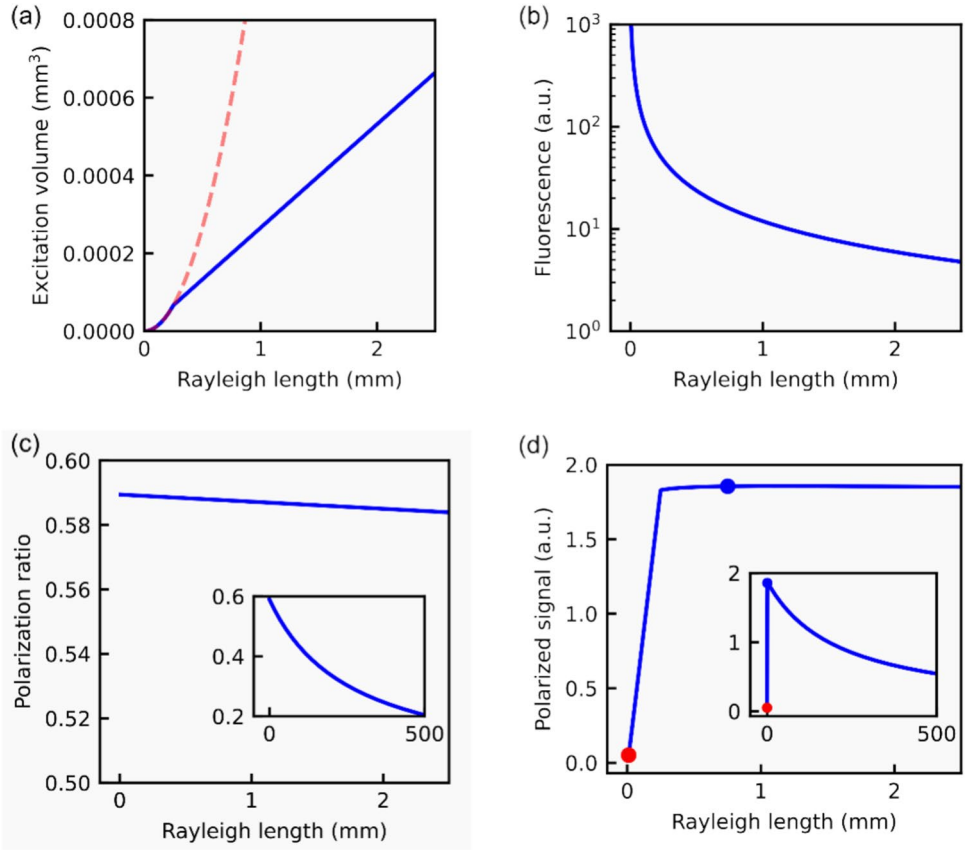

Figure 4. Numerical calculations for a 532 nm laser with a beam diameter of 0.9 mm at a laser power of 10 mW. (**a**) Dependence of excitation volume on the Rayleigh length for sample thicknesses of 500 μm (solid blue line) and infinity (dashed red line). (**b**) Rayleigh length dependence of fluorescence intensity. (**c**) Rayleigh length dependence of polarization ratio. (inset) A wider view of the Rayleigh length region in (**c**). (**d**) Rayleigh length dependence of the product of excitation volume, fluorescence per unit volume, and polarization ratio. Blue and red circles correspond to the CEFM and CFM cases, respectively. In the case of CEFM, the value is approximately 36 times larger compared to CFM. (inset) A wider view of the Rayleigh length region in (**d**).

is good for the short Rayleigh length corresponding to the narrow waist radius, but the detection volume is so small that this product value becomes very small. The fluorescence intensity increases rapidly until twice the Rayleigh length $2Z_R$ reaches near the thickness of the sample, which corresponds to 500 μm. Then, as the twice the Rayleigh length $2Z_R$ increases further, the product's value decreases, mainly due to the decrease in laser power density (Fig. 4d, inset). Note that this calculation is for overall fluorescence emission. The focus calculation is given in the next subsection.

Consideration of detection ratio and selection of optimal objective lens

In the previous subsection, the total amount of emitted fluorescence was calculated in Fig. 4. This subsection deals with the photon correction efficiency of CEFM system. Practically, we calculate the amount of detected fluorescence, taking into account the focusing performance of the objective lens (Fig. 5a). In this calculation, the beam radius of the incident laser is fixed at 450 μm, so the lens's focal length can be determined from the waist radius w_0. The numerical aperture (NA) was calculated from the focal length and the objective lens radius. The detection ratio was then calculated by comparing the ratio with NA = 1 (Fig. 5b). The amount of detected fluorescence for a laser power of 10 mW is obtained by multiplying the product of the detection volume ($=\pi \times w_0^2 \times$ sample thickness), the amount of fluorescence per unit volume I_{cw}, and the polarization ratio P. Figure 5c shows the detected fluorescence as a function of the Rayleigh length. This simulation shows that the maximum amount of the detected fluorescence occurs when twice the Rayleigh length $2Z_R$ matches the sample thickness d. This result is always valid even if the sample thickness changes (see "Supplemental material" for details). Our designed system can be used without concern for laser power because the Rayleigh length at maximum detected fluorescence is constant in the practical range of laser power (see "Supplemental material" for details).

Based on the results obtained so far, the required focal length of the objective lens for CEFM is

$$F = \frac{D}{2}\sqrt{\frac{\pi z_R}{\lambda}} = \frac{D}{2}\sqrt{\frac{\pi d}{2\lambda}}, \tag{4}$$

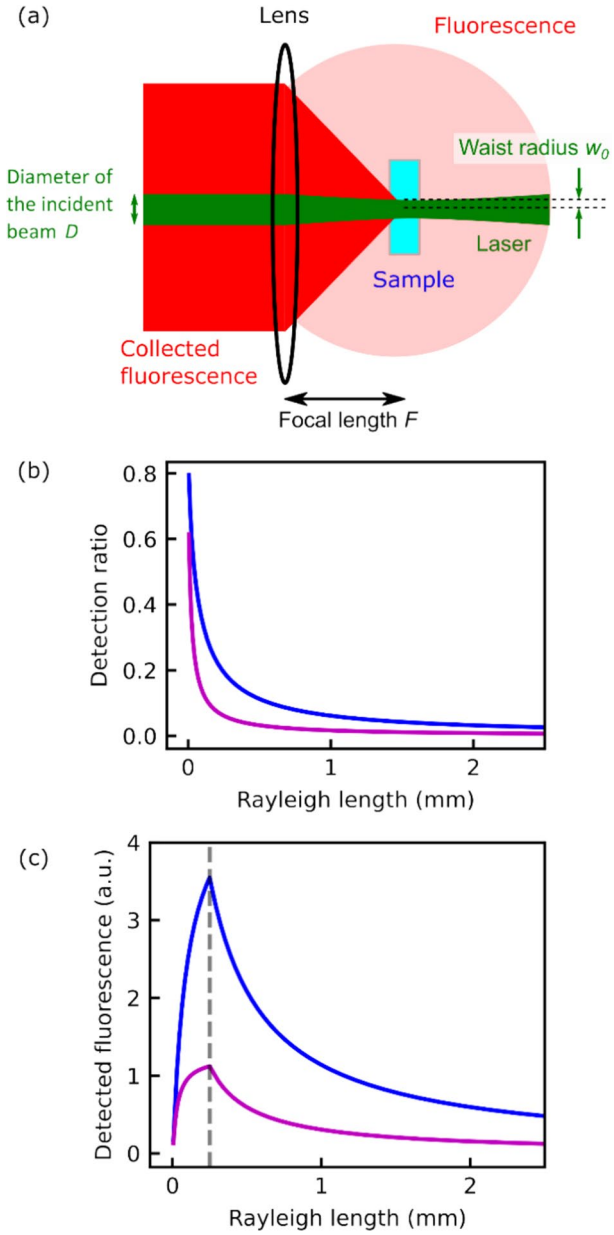

Figure 5. (**a**) Schematic of a sample being excited by a laser and its fluorescence being collected. (**b**) Dependence of detection ratio on excitation Rayleigh length for a 1-inch lens (blue) and a 0.5-inch lens (magenta). (**c**) Dependence of the product of the polarized fluorescence (Fig. 4d) and the detection rate (Fig. 5b) for a 1-inch lens (blue) and a 0.5-inch lens (magenta) on the excitation Rayleigh length at 10 mW laser power. The dashed line represents the location where the Rayleigh length is 0.25 mm, and twice this Rayleigh length $2Z_R$ equals the thickness of the sample.

where D represents the diameter of the incident beam. Here, we use the relationship between the focal length and the waist radius given by $F = \pi w_0 D/2\lambda$. In our experimental setup, the incident beam diameter of the 532 nm laser is 0.9 mm, so we chose the most suitable objective lens focal length from the available choices of commercially available 1-inch achromat lenses is 30 mm.This laser beam, focused by the objective lens with a focal length of F, excites the sample uniformly along the sample thickness and produces a large amount of fluorescence from polarized color centers. Because of the strong collected signal and larger beam spot size, typically about 20 μm, CEFM can measure the spatial distribution of properties throughout the entire millimeter-scale size sample.

Comparison of CEFM and CFM: experimental setup and detection efficiency

We will describe the experimental setup incorporating the objective lens necessary to realize CEFM as explained thus far (Fig. 6a). A significant difference from the typical CFM used in color center experiments is the objective lens we previously showed and the pinhole or the optical fiber functioning as a pinhole. Additionally, depending

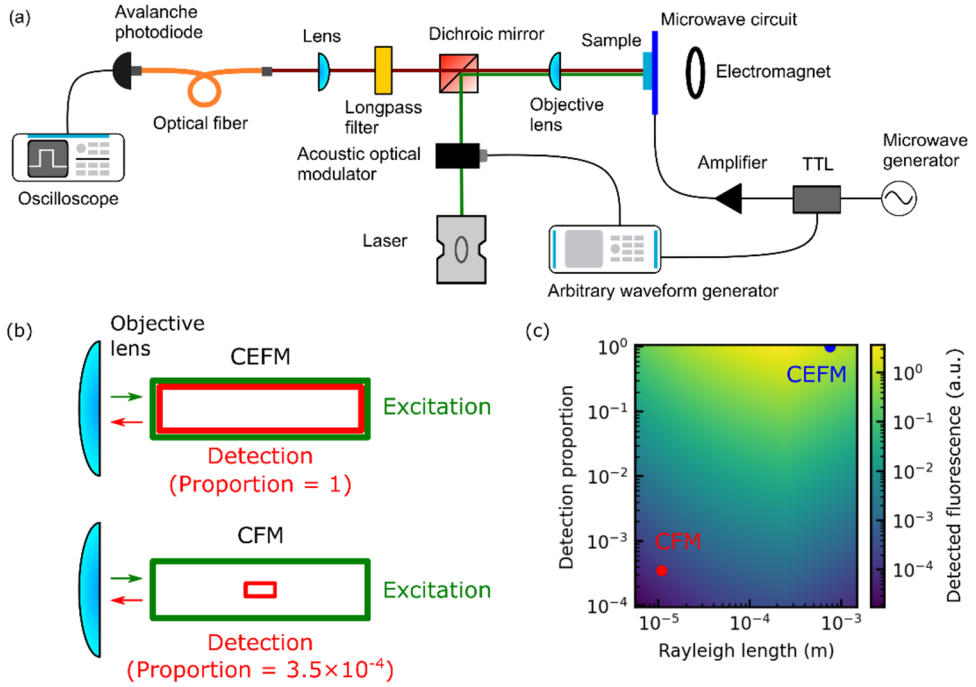

Figure 6. (**a**) Schematic of the experimental setup. (**b**)Schematic comparison of excitation and focusing volumes for confocal microscopy (CFM) and this study. (**c**) Product of polarized fluorescence and detection rate at 10 mW laser power (Fig. 5c) as a function of detection proportion and excitation beam radius. Blue and red circles correspond to CEFM and CFM cases, respectively.

on the concentration of the color center, the amount of light detected is considerably higher than that in CFM, which may necessitate a change in the photodetector and counter (see "Method" section and "Supplemental material" for details). However, except for the items above, all other components are identical to those in CFM. Switching between CEFM and CFM is possible by simply replacing these.

In conventional CFM, the spatial resolution is enhanced due to the presence of the small pinhole and the superior numerical aperture (NA) of the objective lens compared to CEFM. However, the amount of collected fluorescence decreases due to the effect of the pinhole, as indicated by red rectangle in Fig. 6b. The advantage of CEFM is that the measurement time is shortened by making identical sizes between detection and excitation regions, which corresponds to a detection proportion equal to one. The drawback is poor spatial resolution. A large pinhole, which corresponds to optical fiber core in the case of CEFM, makes this large detection proportion possible, as indicated by red and green rectangles in Fig. 6b. The multimode fiber with a core diameter of 200 μm was used in the following experiment.

Compared to CFM with a pinhole diameter of 1 AU, the detected fluorescence of CEFM is more than 10^4 times higher (Fig. 6c). Thus, assuming that the noise levels of both systems are the same, CFM requires 10^8 times the measurement time to achieve the same signal-to-noise ratio as CEFM. In addition, the larger detection volume means that the surface occupies a tiny percentage of the total volume, making it less susceptible to the emission light from impurities and other substances on the surface. Due to the many photons detected, CEFM has a wide concentration range of detectable color centers.

Comparison of measurement signals of CEFM and CFM objective lenses

Figure 7 shows the experimental results of a comparison of the effect of the objective lens on the measurement data using the same measurement system except for the objective lens (see "Method" section for the experimental setup). In Fig. 7a,b, an objective lens that produces a laser beam that fits CEFM design was used, and in Fig. 7c,d, one of the 50× objectives commonly used in CFM (MPLAPON 50× from OLYMPUS) was used. Figure 7a,c show a comparison of pulse ODMR measurements. The solid red lines are Lorenz fittings for the four resonance lines. The leftmost resonance dip in Fig. 7a is the deepest because this transition frequency is closest to the resonance frequency of the microwave circuit. Figure 7b,d show the results of Rabi oscillation measurements. The solid red line is fitting. In the measurement of CEFM, the Rabi contrast is 3%, which is 38 times larger than the standard deviation indicated by the purple error bars (Fig. 7b). On the other hand, in the measurement of CFM, it is difficult to fit the Rabi oscillations, but the signal-to-noise ratio is estimated to be around 1. The signal-to-noise ratio is much lower in Fig. 7c,d than in Fig. 7a,b due to the decrease in fluorescence of the polarized color centers shown in the numerical calculations so far and the conversion from NV^- to NV^0 caused by high laser power density[24,25]. These effects become more pronounced in the case of stronger laser power, but the experiments are impossible because the laser damages the objective lens for CFM.

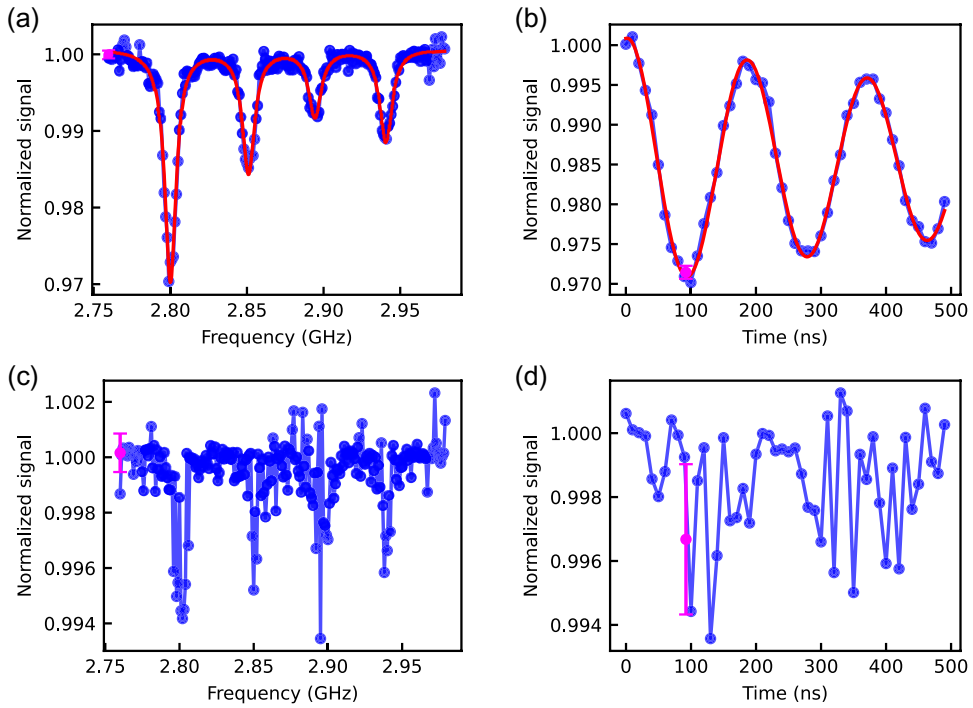

Figure 7. Comparative measurements of ODMR spectrum and Rabi oscillation with CEFM objective lens and a typical objective lens used in CFM. The error bar represents the standard deviation calculated from 100 measurements of the same parameter. (**a**, **b**) Measurements of ODMR spectrum and Rabi oscillation with CEFM objective lens. (**c**, **d**) Corresponding measurements with the typical objective lens used in CFM.

It should be noted that these experimental results compare only the effects of the objective lens, eliminating the influences of signal-to-noise ratio due to differences in photodetectors, among other factors. Therefore, even when using the objective lens for CFM, it cannot demonstrate the excellent spatial resolution of CFM due to the very large pinhole size. In order to utilize the high resolution of CFM, a small pinhole diameter is necessary, and the signal amount in that case corresponds to Fig. 6c. While CFM has the advantage of high spatial resolution, it significantly limits the signal detected, requiring a longer measurement time than CEFM. Also, because CFM has spatial resolution in the depth direction, the evaluation of quantum characteristics of the entire sample with thickness must be inferred from the results of a limited measurement area. On the other hand, CEFM, although it has a lower spatial resolution, can obtain a large amount of fluorescence and evaluate the quantum characteristics across the entire sample, including local defects and distortions, without omission. From these facts, CEFM is particularly effective in cases where a large number of samples need to be evaluated[26,27] or in sensor systems that use the entire sample[28,29].

Measurement of the spatial distribution of the quantum properties

Figure 8 shows the spatial distribution of the quantum properties of NV centers in the diamond. One pixel size is 50 μm × 50 μm, and the spatial measurement area was up to 350 μm × 1050 μm. Here, the x and y coordinates are those shown in Fig. S1b. Figure 8a shows the results of Rabi oscillation measurements at the point (x, y) = (−200um, 100um) of Fig. 8b, fitted by the function $a_1 exp(-\tau/a_2)cos(2\pi a_3\tau + a_4) + a_5$, where τ is the microwave irradiation time, a_i (i = 1–5) is a fitting parameter. Figure 8b shows the spatial distribution of the π pulse duration that inverts the quantum state. This data was used to correct for differences in π pulse duration due to different positions on the microwave circuit, thereby improving the accuracy of the T_1 and T_2 measurements. The π/2 pulse was set to half of the π pulse time. Figure 8c shows the results of the energy relaxation time T_1 measurement at the point (x, y) = (−200um, 100um), fitted by the function $a_1 exp(-\tau/a_2) + a_3$, where τ is the time duration between π pulse and readout, a_i (i = 1–3) is a fitting parameter. In T_1 measurement, π pulses of microwaves were irradiated, and the quantum state was read out as a photoluminescence intensity by a 532 nm laser excitation after a time τ. Figure 8d shows the spatial distribution of the energy relaxation time T_1. The energy relaxation time over the entire measurement region of the sample was (11.0 ± 4.0) ms. Figure 8e is the result of the phase relaxation time T_2 measurement at the point (x, y) = (−200um, 100um), fitted by the function $a_1 exp(-(\tau/a_2)^{a_3})$, where τ is the time between the π pulse and the readout, a_i (i = 1–3) is a fitting parameter. The microwave pulse sequence is π/2 pulse- π pulse—π/2, with π/2 pulse and π pulse separated by time τ. After an exposure of the microwave pulse sequence, the quantum states were read out with a 532 nm laser. We have concluded that the deviation from the fitting function might be the revival caused by the spin bus[30]. Figure 8f shows the spatial distribution of the phase relaxation time T_2. The phase relaxation time over the entire measurement region of the sample was (21.5 ± 1.9) us. The value of T_2. is gradually decreasing from the left-side area to the right-side area. This trend of T_2 spatial distribution corresponds to the trend of the spatial distribution

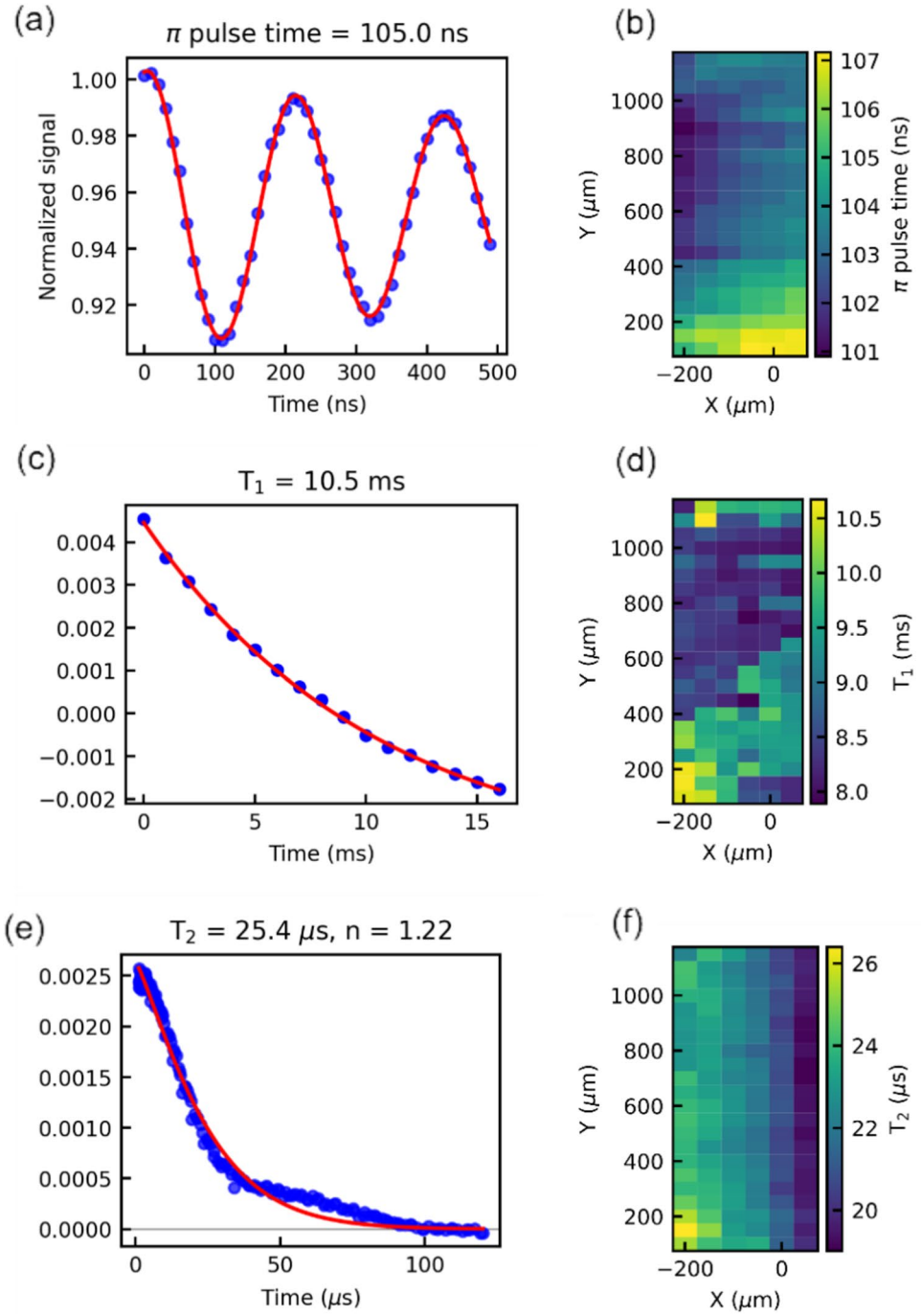

Figure 8. (**a**) Rabi oscillation measurement at the point (x, y) = (−200um, 100um). (**b**) Spatial distribution of π pulse duration. (**c**) Energy relaxation time T_1 measurement at the point (x, y) = (−200um, 100um). (**d**) Spatial distribution of NV center energy relaxation time T_1. (**e**) Phase relaxation time T_2 measured at the point (x, y) = (−200um, 100um). (**f**) Spatial distribution of phase relaxation time T_2 at the NV center.

of fluorescence from the NV^- center, as shown in Fig. S1(b). Figures 8f and S1b indicate that T_2 is decreasing in increasing density of nitrogen and NV^- center as a decoherence source.

Conclusion

In summary, we have developed a method to rapidly measure the sample information such as quantum properties of an entire millimeter-scale sample by constructing a fluorescence microscope with columnar excitation by a long Rayleigh length focused beam. By considering the excitation volume, the polarization ratio of the quantum state, and the detection efficiency, we found that matching twice the Rayleigh length $2Z_R$ to the thickness of the

sample produces the highest amount of detected signal. The detected signal is about 10^4 times larger than the conventional ideal confocal microscopy. CEFM uses an identical microwave setup with conventional confocal microscopy to evaluate color centers. Thus, it is possible to use these microwave pulse sequences for CEFM, such as evaluating NV center density using instantaneous diffusion[31,32]. Density evaluation of spin defects in the quantum material, usually performed on the entire sample by ESR[33], can be accomplished using CEFM, with additional information on spatial distribution. In addition, this method can be used not only for the evaluation of existing color centers, but also for the discovery of new color centers, as it can take advantage of the high signal-to-noise ratio to increase the speed for measuring photoluminescence spectra of unknown color centers[34,35].

Method

A diamond sample containing NV centers was placed on the microwave resonator[29]. The resonator is fixed to a motorized stage with a movable range of 13 mm. A permanent magnet to fix the quantization axis was placed behind the resonator. The strength of the magnetic field was approximately 2.5 mT. The fluorescence from the NV centers was collected through the objective lens (AC254-030-AB-ML; Thorlabs) and detected using an avalanche photodiode (APD410A/M; Thorlabs). An oscilloscope (MDO34; Tektronix) recorded the signal from the avalanche photodiode and analyzed it to distinguish the spin state of the NV centers. Using an arbitrary waveform generator (M3202A; Keysight) to generate the laser and microwave pulse sequence, we controlled an acousto-optic modulator (#35 250-0.2-0.53-XQ; Gooch & Housego) and a transistor-transistor logic (TTL) switch. After the microwave pulse sequence, a 180 μs measurement laser pulse of 532 nm laser (gem 532; Laser Quantum) for measurement with 12 mW was irradiated to the NV centers in the diamond. The diamond {111} single crystal grown by high-temperature/high-pressure (HPHT) synthetic method was used in this study[36]. The HPHT samples were irradiated with a 2.0 MeV electron beam with a total fluence of 5.0×10^{17} cm^{-2} for creating vacancies in the crystal and then annealed at 1000 °C for 2 h in vacuum to create NV centers (see "Supplemental material" for details).

Alternatively, the detector can be an imaging camera if high spatial resolution is needed, although we used an APD in this study. However, an imaging camera requires a dark room and excitation light shielding because the optical fiber used in this system cannot block stray light. In addition, the detected fluorescence per unit pixel is much lower than with a single APD. These effects result in a more extensive setup, increased measurement time, and a lower signal-to-noise ratio. Note that the excitation beam diameter must follow the calculation protocol in this study. Otherwise, unpolarized color center fluorescence reduces the signal-to-noise ratio. For example, this effect can be observed by reduced Rabi contrast (see "Supplemental material" for details).

Data availability

The data that support the findings of this study are available from the corresponding author upon reasonable request.

Received: 29 January 2023; Accepted: 25 July 2024
Published online: 05 August 2024

References

1. Taylor, J. M. *et al.* High-sensitivity diamond magnetometer with nanoscale resolution. *Nat. Phys.* **4**, 810 (2008).
2. Doherty, M. W. *et al.* The nitrogen-vacancy colour centre in diamond. *Phys. Rep.* **528**, 1 (2013).
3. Rondin, L. *et al.* Magnetometry with nitrogen-vacancy defects in diamond. *Rep. Prog. Phys.* **77**, 056503 (2014).
4. Degen, C. L., Reinhard, F. & Cappellaro, P. Quantum sensing. *Rev. Mod. Phys.* **89**, 035002 (2017).
5. Tarasenko, S. A. *et al.* Spin and optical properties of silicon vacancies in silicon carbide: A review. *Physica Status Solidi* **255**, 1700258 (2018).
6. Zhang, G., Cheng, Y., Chou, J.-P. & Gali, A. Material platforms for defect qubits and single-photon emitters. *Appl. Phys. Rev.* **7**, 031308 (2020).
7. Hoang, T. M. *et al.* Thermometric quantum sensor using excited state of silicon vacancy centers in 4H-SiC devices. *Appl. Phys. Lett.* **118**, 044001 (2021).
8. Fescenko, I. *et al.* Diamond magnetometer enhanced by ferrite flux concentrators. *Phys. Rev. Res.* **2**, 023394 (2020).
9. Barry, J. F., Steinecker, M. H., Alsid, S. T., Majumder, J., Pham, L. M., O'Keefe, M. F., Braje, D. A. Sensitive AC and DC magnetometry with nitrogen-vacancy center ensembles in diamond. arXiv preprint arXiv:2305.06269, 2023.
10. Barry, J. F. *et al.* Sensitivity optimization for NV-diamond magnetometry. *Rev. Mod. Phys.* **92**, 015004 (2020).
11. Zhang, C. *et al.* Diamond magnetometry and gradiometry towards subpicotesla dc field measurement. *Phys. Rev. Appl.* **15**, 064075 (2021).
12. Masuyama, Y. *et al.* Gradiometer using separated diamond quantum magnetometers. *Sensors* **21**, 977 (2021).
13. Chen, E. H., Gaathon, O., Trusheim, M. E. & Englund, D. Wide-field multispectral super-resolution imaging using spin-dependent fluorescence in nanodiamonds. *Nano Lett.* **13**, 2073 (2013).
14. Glenn, D. R. *et al.* Single-cell magnetic imaging using a quantum diamond microscope. *Nat. Methods* **12**, 736 (2015).
15. Fescenko, I. *et al.* Diamond magnetic microscopy of malarial hemozoin nanocrystals. *Phys. Rev. Appl.* **11**, 034029 (2019).
16. Lamichhane, S. *et al.* Nitrogen-vacancy magnetometry of individual Fe-triazole spin crossover nanorods. *ACS nano* **17**, 8694 (2023).
17. Kehayias, P. *et al.* Imaging crystal stress in diamond using ensembles of nitrogen-vacancy centers. *Phys. Rev. B* **100**, 174103 (2019).
18. Simpson, D. A. *et al.* Electron paramagnetic resonance microscopy using spins in diamond under ambient conditions. *Nat. Commun.* **8**, 458 (2017).
19. Mizuno, K., Ishiwata, H., Masuyama, Y., Iwasaki, T. & Hatano, M. Simultaneous wide-field imaging of phase and magnitude of AC magnetic signal using diamond quantum magnetometry. *Sci. Rep.* **10**, 11611 (2020).
20. Lamichhane, S., Timalsina, R., Schultz, C., Fescenko, I., Ambal, K.,Liou, S.-H., Lai, R.Y. & Laraoui, A. Detection of iron in nano-clustered cytochrome c proteins using nitrogen-vacancy magnetic relaxometry. arXiv preprint arXiv:2310.08605 (2023)
21. Meschede, D. *Optics, Light and Lasers: The Practical Approach to Modern Aspects of Photonics and Laser Physics* (John Wiley & Sons, 2017).

22. Ahmadi, S., El-Ella, H. A. R., Hansen, J. O. B., Huck, A. & Andersen, U. L. Pump-enhanced continuous-wave magnetometry using nitrogen-vacancy ensembles. *Phys. Rev. Appl.* **8**, 034001 (2017).
23. El-Ella, H. A. R., Ahmadi, S., Wojciechowski, A. M., Huck, A. & Andersen, U. L. Optimised frequency modulation for continuous-wave optical magnetic resonance sensing using nitrogen-vacancy ensembles. *Opt. Express* **25**, 14809 (2017).
24. Manson, N. B. & Harrison, J. P. Photo-ionization of the nitrogen-vacancy center in diamond. *Diamond Relat. Mater.* **14**, 1705 (2005).
25. Acosta, V. M. *et al.* Diamonds with a high density of nitrogen-vacancy centers for magnetometry applications. *Phys. Rev. B* **80**, 115202 (2009).
26. Shinei, C. *et al.* Nitrogen related paramagnetic defects: Decoherence source of ensemble of NV- center. *J. Appl. Phys.* **132**, 214402 (2022).
27. Teraji, T., Shinei, C., Masuyama, Y., Miyakawa, M. & Taniguchi, T. Nitrogen concentration control during diamond growth for NV- centre formation. *Philos. Trans. R. Soc. A* **382**, 20220322 (2024).
28. Clevenson, H. *et al.* Broadband magnetometry and temperature sensing with a light-trapping diamond waveguide. *Nat. Phys.* **11**, 393 (2015).
29. Masuyama, Y. *et al.* Extending coherence time of macro-scale diamond magnetometer by dynamical decoupling with coplanar waveguide resonator. *Rev. Sci. Instrum.* **89**, 125007 (2018).
30. Childress, L. *et al.* Coherent dynamics of coupled electron and nuclear spin qubits in diamond. *Science* **314**, 281 (2006).
31. Klauder, J. R. & Anderson, P. W. Spectral diffusion decay in spin resonance experiments. *Phys. Rev.* **125**, 912 (1962).
32. Schweiger, A. & Jeschke, G. *Principles of Pulse Electron Paramagnetic Resonance* (Oxford University Press, 2001).
33. Ishii, S. *et al.* Ensemble negatively-charged nitrogen-vacancy centers in type-Ib diamond created by high fluence electron beam irradiation. *Quantum Beam Sci.* **6**, 2 (2021).
34. Wolfowicz, G. *et al.* Quantum guidelines for solid-state spin defects. *Nat. Rev. Mater.* **6**, 906 (2021).
35. Kanai, S. *et al.* Generalized scaling of spin qubit coherence in over 12,000 host materials. *Proc. Natl. Acad. Sci.* **119**, e2121808119 (2022).
36. Miyakawa, M., Shinei, C. & Taniguchi, T. Nitrogen concentration control in diamonds grown in Co–(Fe)–Ti/Al solvents under high-pressure and high-temperature. *Jpn. J. Appl. Phys.* **61**, 045507 (2022).

Acknowledgements

This work was supported by MEXT Q-LEAP (JPMXS0118067395 and JPMXS0118068379). YM acknowledges the support of JSPS KAKENHI (20K14392). T.T. acknowledges the support of JST Moonshot R&D (JPMJMS2062), MIC R&D for construction of a global quantum cryptography network (JPMI00316) and JSPS KAKENHI (20H02187, 20H05661).

Author contributions

The measurement system was designed, constructed, and tested by Y.M. Y.M. and C.S. performed the measurements and the data analysis. T.T. synthesized the diamond. The diamond was electron-irradiated by S. I. and H.A. The overall supervision was performed by T.T. and T.O.

Competing interests

The authors declare no competing interests.

Additional information

Supplementary Information The online version contains supplementary material available at https://doi.org/10.1038/s41598-024-68610-5.

Correspondence and requests for materials should be addressed to Y.M.